In: Solar Wind: Effects, Dynamics and Interactions ISBN 0000000000
Editor: Frank Columbus, pp. 1-20 

***Chapter 1***

# SOLAR WIND INTERACTION WITH ARTIFICIAL ATMOSPHERES

***L. Gargaté***[1,*]***, R. A. Fonseca***[1,2]***, R. Bamford***[3]***, R. Bingham***[3]***, L. O. Silva***[1]
[1]GoLP/Instituto de Plasmas e Fusão Nuclear,
Instituto Superior Técnico, Av. Rovisco Pais, 1049-001 Lisbon, Portugal
[2]DCTI, Instituto Superior de Ciências do Trabalho e da Empresa,
Av. Forças Armadas, 1649-026 Lisbon, Portugal
[3]Space Science & Technology Dept,Science & Technology Facilities Council,
Rutherford Appleton Laboratory, Harwell Science and Innovation Campus,
Didcot, Oxon, OX11 0QX UK

**Abstract**

Active experiments in space involving artificial atmospheres began with the AMPTE releases. In these seminal experiments, a cloud of Barium or Lithium was released and photoionized by the UV radiation from the sun. The cloud expanded and interacted with flowing solar wind, thus providing important data about pick-up ion behaviour, diamagnetic cavity formation, and shock formation. More recently, systems consisting of a dipole magnetic field and a plasma source are being considered and studied in spacecraft propulsion, and as a spacecraft shield from Solar Energetic Particles (SEP) from the sun [1].

We use a 3D massively parallel hybrid code to analyze the behaviour of such systems in the presence of a plasma flow. The model is ideal to deal with artificial atmospheres interacting with the solar wind, covering the relevant physical scales, and allowing a kinetic treatment of the ions. The code allows for arbitrary density distributions, arbitrary initial velocity distributions, and particle injection at any point in the simulation box. Dynamic load balancing algorithms are also used to guarantee parallel efficiency.

We focus our analysis in the differences between two distinct scenarios: the unmagnetized scenario of a plasma cloud expanding in the solar wind in the presence of the Interplanetary Magnetic Field (IMF), and the magnetized scenario of a laboratory plasma flow shock against a dipole magnetic field structure. Our results show that both configurations effectively deflect the incoming plasma. The nature of the shocks

*E-mail address: luisgargate@ist.utl.pt

formed in both situations is different, a bow shock being formed in the first case, while in the second case there is a compression of the magnetic field, but no bow shock is observed. In the unmagnetized case, the diamagnetic cavity formation is the most significant aspect, with the cloud particles producing the diamagnetic currents as they expand outwards due to their temperature. Our results also show a dependency of the plasma standoff distance with the plasma density, velocity, and with the dipole field intensity in the magnetized case. The relevance of these scenarios for the shielding of spacecrafts is also addressed.

**Key Words**: artificial magnetospheres, solar wind, shocks, numerical simulations

# 1 Introduction

Active space experiments and in-situ measurements by satellites in space are important to understand the solar wind, the solar wind interaction with magnetospheres or planetary exospheres, and the space environment in general. Important phenomena like the rarefaction of the Martian atmosphere, the onset of geomagnetic storms, and the interaction of large-scale structures (e.g. Coronal Mass Ejections, Interplanetary Shocks) with the Earth's magnetosphere, are better understood today thanks to numerous space missions, and to many developments in theoretical knowledge, computing power, and simulation techniques.

The increase of computing power and the improvement of the simulation techniques has led to a renewed interest in specific space plasma problems that can now be tackled with MHD codes, hybrid codes (with kinetic ions and fluid electrons), and fully kinetic codes. One interesting problem is the interaction of the solar wind with artificial magnetospheres, either in the traditional sense of a magnetosphere dominated by a dipole magnetic field, or of a plasma cloud expanding in the solar wind. Of particular interest is the possibility of using such artificial magnetospheres to protect spacecrafts against high-energy particles, mostly SEPs, motivated by recent results in the field suggesting the viability of such strategies [1].

Solar Energetic Particles are charged particles originating from the sun, mostly protons and electrons, that can reach energies up to hundreds of $\mathrm{MeV}$ or even $\mathrm{GeV}$ in some extreme scenarios. These SEP particles are hazardous to both spacecrafts (e.g. electronics, external panels), and to astronauts in space. The concept of spacecraft protection using artificial magnetospheres is then an attempt to emulate what the Earth magnetosphere does naturally for our planet, using a small scale dipole field and a plasma source to create a shield against charged particles.

Similar plasma cloud and magnetic field configurations have also been considered for spacecraft propulsion in the Solar System [2–4]. In that context, experimental [5–8] and simulation work has recently been performed, including detailed numerical simulations of the expansion of a magnetic bubble in the absence of a plasma flow [9, 10].

A comprehensive study of how high energy particles are deflected by a magnetosphere has not yet been completed. It is an intricate problem, and even in the well studied case of the Earth, a full understanding of the mechanisms responsible for effective SEP deflection is lacking: while it is known that some very energetic particles (tens of MeVs) penetrate the magnetopause and are trapped in the Earth radiation belt for very long periods, the physical processes relevant for particle transport across the magnetopause are still a central object of investigation.

We base the first part of our study on the analysis of the interaction of the solar wind with an unmagnetized plasma cloud, adopting parameters that allow for a comparison of our results with the measurements from the AMPTE release experiments, as well as with previous results from the numerical modeling of these experiments [11–16]. The AMPTE experiments consisted of several gas (Lithium and Barium) releases in the upstream solar wind by a spacecraft orbiting the earth [17–19]. After the release, the expanding cloud of atoms is photoionized by the solar ultraviolet radiation, thus producing an expanding plasma and forming an obstacle to the flowing solar wind. In-situ measurements were made by two additional spacecrafts and observations from ground-based stations were also performed.

The problem is intrinsically kinetic in nature due to the fact that the Larmor radius of the ions is of the order of magnitude of the plasma cloud size. Furthermore, modeling the ion kinetics correctly is essential to understand how the solar wind ions are deflected around the plasma cloud. While MHD simulations do not capture kinetic effects, fully kinetic simulations are computationally too demanding. In this sense, the hybrid technique is ideal to model the problem, since the relevant ion kinetics is captured, while high electron-scale frequencies and associated phenomena are neglected. We describe the most important features of the interaction, including the magnetic field buildup in front of the shock, the formation of a diamagnetic cavity, the solar wind behavior around the cloud expansion zone, and the main distinctive features of the cloud expansion itself.

The second part of our study focuses on the deflection of a plasma beam by a mini-magnetosphere in the laboratory, and is directly comparable to laboratory experiments currently underway [8]. In these experiments, a plasma beam, guided by an axial magnetic field in a cylindrical linear chamber, hits a dipole magnetic field created by a permanent magnet. Recent experimental and simulation results reveal the formation of a very sharp shock structure, and provide evidence of the beam deflection out of the magnetized cavity [1]. Modeling the ion kinetics is crucial in this case too, although the plasma can become magnetized in the regions adjacent to the dipole magnetic field origin, due to the sharp gradient in the magnetic field intensity of a dipole $B \sim r^{-3}$. In order to understand the key parameters that determine the mini-magnetosphere features, a parameter scan of the plasma density, the flow velocity and the dipole magnetic field intensity has been performed, giving a particular emphasis to the shock behavior, the distance of magnetopause to the dipole field origin, and the behavior of the beam around the plasma-depleted region of the magnetic dipole.

We resort to hybrid simulations of the two scenarios, the case of the plasma cloud expanding in the solar wind, and the case of the magnetic dipole field interaction with a laboratory plasma beam, to analyze and to compare the features of both systems. A particle-in-cell [20, 21] hybrid code, *dHybrid* [22], is used for the modeling, and the visualization is performed with the osiris framework [23]; *dHybrid* is a massively parallel three-dimensional kinetic ion, massless fluid electron code [24], allowing for arbitrary plasma configurations, external fields, and implementing a particle tracking algorithm that allows for individual particle information to be stored and analyzed.

In the next section we describe the hybrid simulation model in detail, including the implementation in *dHybrid*, and the main features of the code. In section 3 we present the results of the unmagnetized plasma cloud expanding in the solar wind, and in section 4 we present the results of the magnetized laboratory scenario. Finally, in section 5, we present the conclusions.

# 2 The hybrid simulation model

## 2.1 The hybrid model

Hybrid models are commonly used in many problems in plasma physics, and can include different types of approximations, depending on the specific physical system considered [24]. The main assumption of hybrid models with kinetic ions and fluid electrons is that the dynamic scales of interest are those of the ions, while the dynamics of the electrons can be neglected to a lesser or higher degree. This translates in neglecting the displacement current in Ampère's Law, thus suppressing the propagation of electromagnetic waves traveling at the speed of light, and considering an MHD model for the electrons, as well as assuming quasi-neutrality. Differences between various hybrid approximations depend mainly on whether the effects of finite electron mass, resistivity, and electron pressure need to be included in the MHD equations. For the sake of completeness we present the main steps in the derivation of the hybrid model implemented in *dHybrid*.

We start from the Vlasov equation for the electrons,

$$\frac{\partial f_e}{\partial t} + \vec{v}_e \cdot \vec{\nabla}_r f_e - \frac{e}{m}\left(\vec{E} + \vec{v}_e \times \vec{B}\right) \cdot \vec{\nabla}_{v_e} f_e = 0 \tag{1}$$

where $f_e$ is the electron distribution function, $\vec{v}_e$ is the electron velocity, $\vec{E}$ the electric field, $\vec{B}$ the magnetic field, $e$ and $m$ the electron charge and the electron mass, and $\vec{\nabla}_r$ and $\vec{\nabla}_{v_e}$ denote the gradients in physical space and in velocity space, respectively. The zeroth order moment is calculated by integrating eq. 1 in velocity space, the first term from the left yielding $\frac{\partial n}{\partial t}$, with $n = \int f_e \mathrm{d}\vec{v}_e$ the electron density, the second term yielding $\vec{\nabla}_r \cdot \int \vec{v}_e f_e \mathrm{d}\vec{v}_e$, and the last term vanishing if we integrate by parts and make the usual assumption $f_e \rightarrow 0$ at $\pm\infty$.

In the current version of *dHybrid*, the effects of finite electron mass, resistivity and electron pressure are not considered, although the code is already structured so as to make such generalization straightforward. In the $m \rightarrow 0$ limit, eq. 1, which yields the continuity equation for the zeroth order moment, reduces to

$$\left(\vec{E} + \vec{v}_e \times \vec{B}\right) \cdot \vec{\nabla}_{v_e} f_e = 0 \tag{2}$$

and its zeroth order moment is identically zero. The first order moment of eq. 2 is

$$\int \vec{v}_e \left(\vec{E} + \vec{v}_e \times \vec{B}\right) \cdot \vec{\nabla}_{v_e} f_e \mathrm{d}\vec{v}_e = 0$$
$$\Longleftrightarrow \int \vec{v}_e \vec{\nabla}_{v_e} \cdot \left[f_e \left(\vec{E} + \vec{v}_e \times \vec{B}\right)\right] \mathrm{d}\vec{v}_e - \int \vec{v}_e f_e \vec{\nabla}_{v_e} \cdot \left(\vec{E} + \vec{v}_e \times \vec{B}\right) \mathrm{d}\vec{v}_e = 0 \tag{3}$$

where we have used the vector identity $\vec{\nabla} \cdot \left(f\vec{A}\right) = \vec{A} \cdot \vec{\nabla} f + f \vec{\nabla} \cdot \vec{A}$. The second integral of eq. 3 vanishes since $\vec{\nabla}_{v_e} \cdot \left(\vec{E} + \vec{v}_e \times \vec{B}\right) = 0$, while the first integral of eq. 3 is calculated by parts, the non-vanishing term yielding

$$\int f_e \left(\vec{E} + \vec{v}_e \times \vec{B}\right) \mathrm{d}\vec{v}_e = 0$$
$$\Longleftrightarrow \vec{E} = -\vec{V}_e \times \vec{B} \tag{4}$$

with $\vec{V}_e = \frac{1}{n} \int f_e \vec{v}_e \mathrm{d}\vec{v}$ the electron fluid velocity. This last equation indicates that the electric field is perpendicular to the local magnetic field, and results from considering zero inertia electrons that instantaneously short-circuit any parallel component of the electric field.

In the hybrid approximation we now consider Ampère's law without the displacement current

$$\vec{\nabla} \times \vec{B} = \mu_0 \vec{J} \tag{5}$$

where $\mu_0$ is the magnetic permeability, $J$ is the current density, and where $\nabla$ is the usual gradient in physical space, to be used instead of $\nabla_r$ from now on. The current is given by

$$\vec{J} = -n\, e\, \vec{V}_e + \sum_{i=1}^{n_{sp}} q_i \int f_i \vec{v}_i \mathrm{d}\vec{v}_i \tag{6}$$

with $q_i$ the charge of species $i$, and where the sum is over all ion species present in the system. Substituting $\vec{V}_e$ from eq. 6 in eq. 4, and $\vec{J}$ from eq. 5 in eq. 6, the electric field becomes

$$\vec{E} = -\vec{V}_i \times \vec{B} + \frac{1}{ne\mu_0} \left(\nabla \times \vec{B}\right) \times \vec{B} \tag{7}$$

where $\vec{V}_i = \frac{1}{n} \sum_{j=1}^{n_{sp}} Z_j \int f_j \vec{v}_j \mathrm{d}\vec{v}_j$ is the ion fluid velocity, $Z_j = q_j/e$ is the relative charge of the ion species $j$, and where we have assumed quasi-neutrality, $n = \sum_{j=1}^{n_{sp}} Z_j n_j$.

Finally, the magnetic field can be obtained straightforwardly from Faraday's law

$$\frac{\partial \vec{B}}{\partial t} = -\vec{\nabla} \times \vec{E} \tag{8}$$

while the ion velocities are determined by the Lorentz force equation

$$\frac{\mathrm{d}\vec{v}_i}{\mathrm{d}\, t} = \frac{q_i}{M} \left(\vec{E} + \vec{v}_i \times \vec{B}\right) \tag{9}$$

and the ion positions are determined from

$$\frac{\mathrm{d}\vec{x}}{\mathrm{d}\, t} = \vec{v}_i \tag{10}$$

where $M$ is the mass of the ions and $x$ the position of the ions. Equations 4 through 10 form the basis of the hybrid model implemented in *dHybrid*; the numerical method for the solution of this set of equations is described in the next paragraphs.

### 2.2 Implementation in *dHybrid*

The ion species in *dHybrid* are represented by finite sized computational particles to be pushed in a 3D simulation box. The fields and fluid quantities, such as the density $n$ and the ion fluid velocity $\vec{V}_i$, are interpolated from the particles using quadratic splines [25] and defined on two different 3D regular staggered grids [26]. The fields and fluid quantities are then interpolated back to push the ions using quadratic splines, in a self-consistent manner.

All quantities are expresseed in normalized units: time is normalized to the inverse cyclotron frequency $\omega_{ci}^{-1}$, space is normalized to $c/\omega_{pi}$, with $\omega_{pi}$ the ion plasma frequency, charge is normalized to the proton charge $e$, the mass is normalized to the proton mass, and the velocities are normalized to the Alfvèn velocity $v_A = B_0/\sqrt{\mu_0 n_0 m_p}$, where $B_0$ is the normalizing magnetic field, $n_0$ the normalizing density, and $m_p$ the proton mass. In these units, eq. 7 through eq. 10 can be rewritten, dropping the index $i$ for the ions, as

$$\vec{E} = -\vec{V} \times \vec{B} + \tfrac{1}{n}\left(\nabla \times \vec{B}\right) \times \vec{B} \tag{11}$$

$$\frac{\partial \vec{B}}{\partial t} = -\vec{\nabla} \times \vec{E} \tag{12}$$

$$\frac{\mathrm{d}\vec{v}}{\mathrm{d}\,t} = \tfrac{q}{M}\left(\vec{E} + \vec{v} \times \vec{B}\right) \tag{13}$$

$$\frac{\mathrm{d}\vec{x}}{\mathrm{d}\,t} = \vec{v} \tag{14}$$

The equations are advanced in time in finite steps $\Delta t$, and are discretized in space on the two staggered grids, grid $1/2$ being displaced from grid $1$ by half cell size in each spacial direction ($\Delta x/2$, $\Delta y/2$, and $\Delta z/2$). Any quantity $A$ can be transposed from one grid to the other by spatial averaging:

$$\begin{aligned} &A_{i+1/2,j+1/2,k+1/2} = \\ &\frac{1}{8}\left(A_{i,j,k} + A_{i+1,j,k} + A_{i,j+1,k} + A_{i+1,j+1,k} + \right. \\ &\left. A_{i,j,k+1} + A_{i+1,j,k+1} + A_{i,j+1,k+1} + A_{i+1,j+1,k+1}\right) \end{aligned} \tag{15}$$

Derivatives are calculated by the finite differences method in order to be space centered; hence, calculating $\frac{\partial A}{\partial x}$, would yield

$$\begin{aligned} &\left(\frac{\partial A}{\partial x}\right)_{i+1/2,j+1/2,k+1/2} = \\ &= \frac{1}{4\Delta x}\left(A_{i+1,j,k} - A_{i,j,k} + A_{i+1,j+1,k} - A_{i,j+1,k} \right. \\ &\left. + A_{i+1,j,k+1} - A_{i,j,k+1} + A_{i+1,j+1,k+1} - A_{i,j+1,k+1}\right) \end{aligned} \tag{16}$$

meaning that a given quantity and its derivative are defined on different grids [24]. Following this approach, the field equations 11 and 12 are solved numerically by the Lax-Wendroff algorithm [21, 24], which is then second order accurate in space and time, and is space and time centered. The electric field is calculated in two steps:

$$\vec{E}_{1/2}^{n+1/2} = -\vec{V}_{1/2}^{n+1/2} \times \vec{B}_{1/2}^{n+1/2} + \frac{1}{n_{1/2}^{n+1/2}}\left(\vec{\nabla} \times \vec{B}_1^{n+1/2}\right)_{1/2} \times \vec{B}_{1/2}^{n+1/2} \tag{17}$$

$$\vec{E}_1^{n+1} = 2\vec{E}_1^{n+1/2} - \vec{E}_1^{n} \tag{18}$$

the superscripts $n+1/2$ and $n+1$ denoting quantities calculated at times $t_{n+1/2} = t_n + \Delta t/2$, and at times $t_{n+1} = t_n + \Delta t$, and the subscripts 1 and $1/2$ denoting quantities defined on grid 1 at the point $i, j, k$ and on grid $1/2$ at the point $i+1/2, j+1/2, k+1/2$. While eq. 17 is a direct discretization of eq. 11, eq. 18 uses values from eq. 17 displaced from grid $1/2$, and uses the electric field from the previous time step. The magnetic field is advanced in time through

$$\vec{B}_{1/2}^{n+1/2} = \vec{B}_{1/2}^{n} - \tfrac{\Delta t}{2}\left(\vec{\nabla} \times \vec{E}_1^n\right)_{1/2} \tag{19}$$

$$\vec{B}_1^{n+1} = \vec{B}_1^n - \Delta t\left(\vec{\nabla} \times \vec{E}_{1/2}^{n+1/2}\right)_1 \tag{20}$$

Finally, the Boris pusher scheme [21, 27] is used to advance the velocities in time; eq. 13 becomes

$$\vec{v}^{-} = \vec{v}^{n+1/2} + \vec{E}_{1/2}^{n+1}\left(\frac{\Delta t\, q}{2M}\right) \tag{21a}$$

$$\vec{v}^{\prime} = \vec{v}^{-} + \vec{v}^{-} \times \vec{B}_{1/2}^{n+1}\left(\frac{\Delta t\, q}{2M}\right) \tag{21b}$$

$$\vec{v}^{+} = \vec{v}^{-} + \vec{v}^{\prime} \times \vec{B}_{1/2}^{n+1}\left(\frac{\Delta t\, q}{2M}\frac{2}{1+\left|\vec{B}_{1/2}^{n+1}\right|^2\left(\frac{\Delta t q}{2M}\right)^2}\right) \tag{21c}$$

$$\vec{v}^{n+3/2} = \vec{v}^{+} + \vec{E}_{1/2}^{n+1}\left(\frac{\Delta t\, q}{2M}\right) \tag{21d}$$

and the discretization of eq. 14, for the position update, yields

$$\vec{x}^{n+3/2} = \vec{x}^{n+1/2} + \Delta t\, \vec{v}^{n+1} \tag{22}$$

where $\vec{v}^{n+1} = 1/2\left(\vec{v}^{n+1/2} + \vec{v}^{n+3/2}\right)$.

The numerical implementation of the hybrid model described above in *dHybrid* is based on the Message Passing Interface (MPI) routines [28]; the use of standard particle-in-cell algorithm optimization schemes [25] along with state-of-the-art dynamic load balancing techniques guarantees excellent parallel scalability up to hundreds of CPUs [22]. The 3D simulation space is divided across processes, and 1D, 2D and 3D domain decompositions are possible. Using the dynamic load balancing capabilities of *dHybrid*, the simulation space is redistributed across processes during any simulation, in order to maintain similar computing loads across nodes; speedups of up to 40% are observed for runs with uneven particle distributions, as in the present case.

The code can simulate an arbitrary number of particle species with arbitrary charge to mass ratios, arbitrary initial thermal velocity and drift velocity distributions, as well as arbitrary spatial configurations. Periodic boundary conditions, open boundary conditions and configurable particle injectors can be used for the particles, and periodic boundary conditions are used for the fields. The code also includes particle tracking capabilities, which are of particular relevance for the problem at hand. To take full advantage of particle tracking, a simulation is typically ran twice: the first time all usual diagnostics can be analyzed (e.g. electric field, magnetic field, fluid phase spaces), and a special kind of diagnostics, the raw

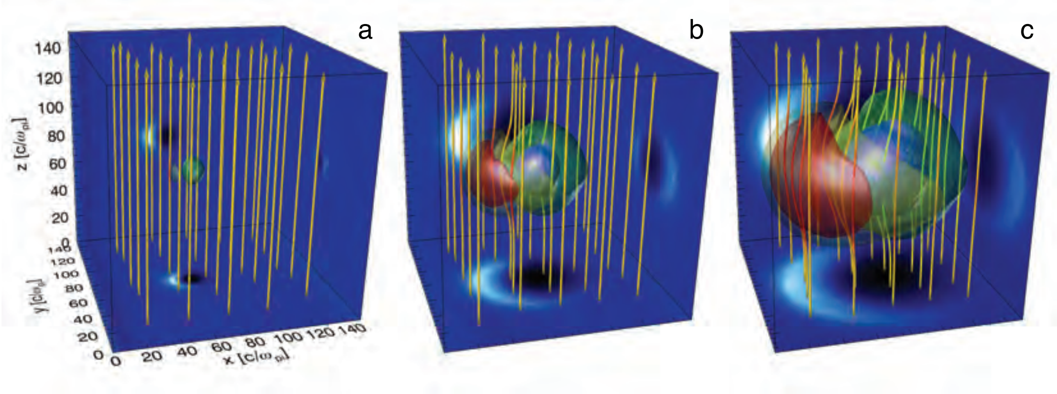


Figure 1: Magnetic field vectors, magnetic field iso-surfaces, and magnetic field projections at a) $t = 2.22$, b) $t = 11.08$, and c) $t = 19.94$.

diagnostics, are produced. In these raw diagnostics, a sample of raw simulation particles is stored at given intervals, including the positions, the velocities and the charge. A sample of these particles is then chosen according to specific, problem-dependent criteria (e.g., particles within a given energy interval and/or spatial region), and the list of particles is supplied as an input for the second run, which then provides a detailed time-resolved information on the phase-space dynamics of the selected particles.

In the physical scenarios considered here, particle tracking allows for the determination of how particles behave near the shock structures formed by the plasma cloud expansion, and by the dipole magnetic field in the laboratory phase.

## 3 Plasma cloud interaction with the solar wind

In the AMPTE release experiments, clouds of Lithium or Barium were released in the upstream solar wind, which is essentially a proton/electron plasma. The gas cloud expanded due to its temperature, while particles were photo-ionized by solar UV radiation. The IMF from the sun was the only external magnetic field source in this case. In our 3D simulation box, the solar wind propagates in the $+x$ direction, the magnetic field is oriented in the $+z$ direction, and a pre-ionized Lithium cloud expands from a point at $40\%$ the box size in the $x$ direction, and centered in the $y$ and $z$ directions.

Results are presented in normalized units, the density normalized to $n_0 = 5\,\mathrm{cm}^{-3}$, the spacial dimensions normalized to $c/\omega_{pi} \approx 102\,\mathrm{km}$, the time normalized to $\omega_{ci}^{-1} \approx 4.53\,\mathrm{s}$, the velocities normalized to $v_A \approx 22.5\,\mathrm{km\,s}^{-1}$, the magnetic field normalized to $B_0 = 2.3\,\mathrm{nT}$, and the electric field normalized to $B_0\,v_A \approx 0.0516\,\mathrm{mV\,m}^{-1}$. The box size is $L = 150\,\mathrm{c}/\omega_{\mathrm{pi}} \approx 15000\,\mathrm{km} \approx 41\,\mathrm{r}_{\mathrm{Lsw}}$ in each dimension, with $r_{Lsw}$ the solar wind Larmor radius, and $(300)^3$ grid cells are used, yielding a cell size of $\Delta = 0.5\,\mathrm{c}/\omega_{\mathrm{pi}} \approx 51\,\mathrm{km} \approx 0.14\,\mathrm{r}_{\mathrm{Lsw}}$. The time step is $\Delta t \approx 0.0022\,\omega_{\mathrm{ci}}^{-1} \approx 0.01\,\mathrm{s} \approx 3.5 \times 10^{-4}\,\mathrm{T}_{\mathrm{Lsw}}$, where $\mathrm{T}_{\mathrm{Lsw}}$ is the solar wind ion gyro period, and the simulation is run up to 10000 time steps, which results in a total simulation time $T \approx 22\,\omega_{\mathrm{ci}}^{-1} \approx 100\,\mathrm{s} \approx 3.51\,\mathrm{T}_{\mathrm{Lsw}}$. We use

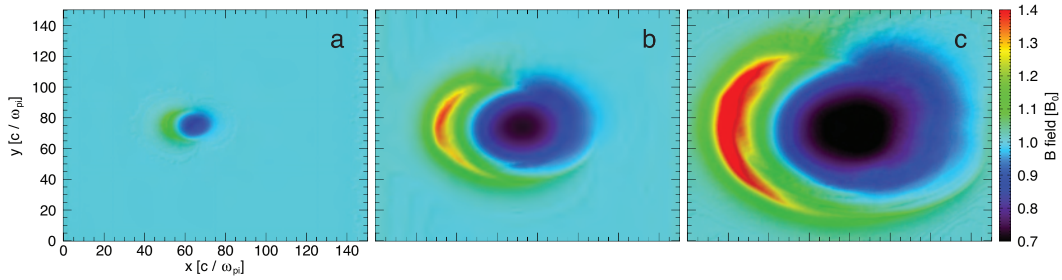


Figure 2: Magnetic field intensity cut along the $x\,y$ plane at $z = 75$ for: a) $t = 2.22$, b) $t = 11.08$, and c) $t = 19.94$.

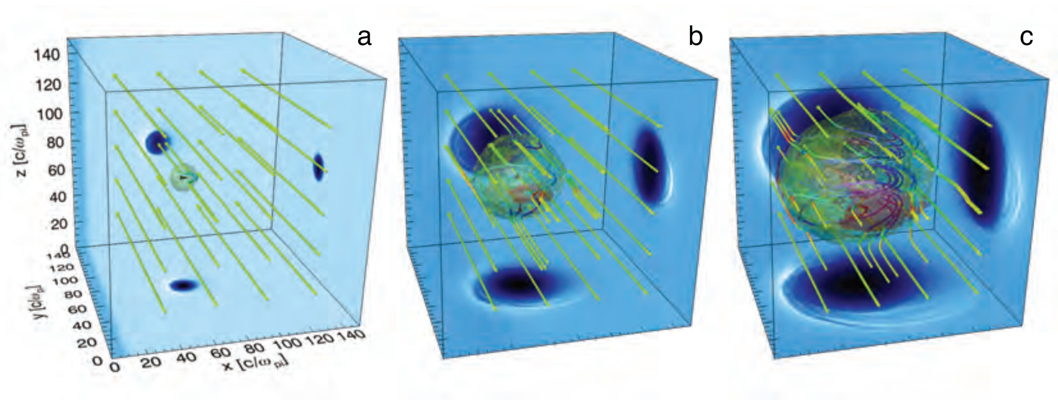


Figure 3: Electric field vectors, electric field iso-surfaces, and electric field projections at a) $t = 2.22$, b) $t = 11.08$, and c) $t = 19.94$.

8 particles per cell to model the solar wind plasma, and around 2 million particles to model the Lithium cloud.

The background magnetic field in the simulation is $B = 1$ $(\approx 2.3\,\mathrm{nT})$, and the solar wind plasma is distributed uniformly across the box with a density $n_{sw} = 1$ $\left(\approx 5\,\mathrm{cm}^{-3}\right)$, a drift velocity of $V_{sw} = 3.59$ $\left(\approx 80.5\,\mathrm{km\,s}^{-1}\right)$, and a temperature of $T = 0.78\,\mathrm{eV}$, yielding a kinetic to magnetic pressure ratio $\beta \approx 0.3$. The Lithium ions in the plasma cloud are singly ionized and are initialized in a sphere of radius $r_{Li} = 4$ with a gaussian density profile with peak density $n_{Li} \approx 56000$, and a temperature $T = 15.5\,\mathrm{eV}$.

The most striking feature of the system is the magnetic field behavior as the cloud expands. Figure 1 shows the magnetic field evolution including the magnetic field vectors, iso-surfaces and projections, and figure 2 shows a $x\,y$ plane cut of the magnetic field intensity at $z = 75$. The magnetic field present at the beginning (frame a) is mostly the IMF field. As the cloud expands, the IMF is pushed out of the cloud expansion zone; the magnetic field vectors are bent, a compression zone is formed in the upstream side of the shock, and a low magnetic field zone, a diamagnetic cavity, is formed in the downstream side of the shock. Figure 2 at later time steps, frames b and c, shows a clear asymmetry between the

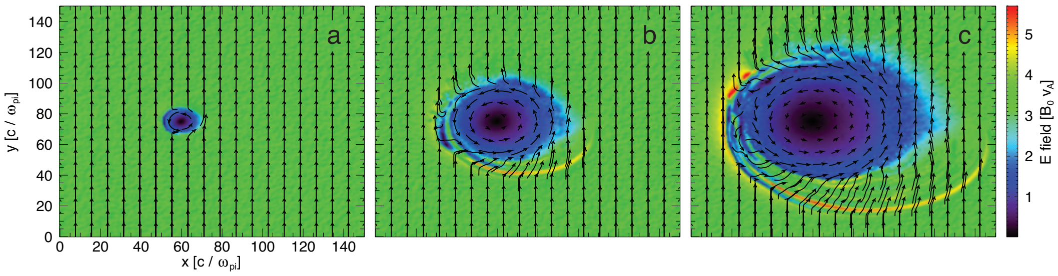


Figure 4: Electric field intensity cut along the $xy$ plane at $z = 75$ for: a) $t = 2.22$, b) $t = 11.08$, and c) $t = 19.94$.

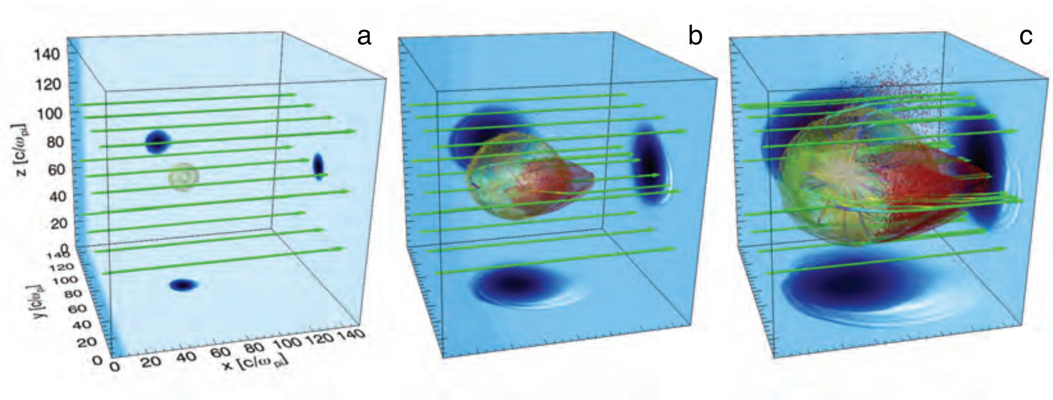


Figure 5: Fluid velocity vectors, fluid velocity iso-surfaces, and fluid velocity projections at a) $t = 2.22$, b) $t = 11.08$, and c) $t = 19.94$.

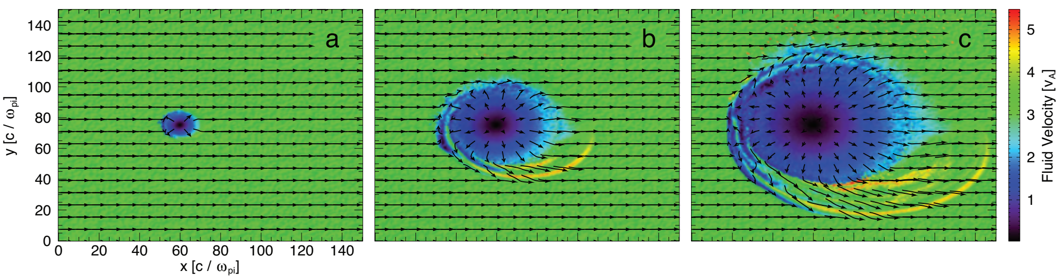


Figure 6: Fluid velocity intensity cut along the $xy$ plane at $z = 75$ for: a) $t = 2.22$, b) $t = 11.08$, and c) $t = 19.94$.

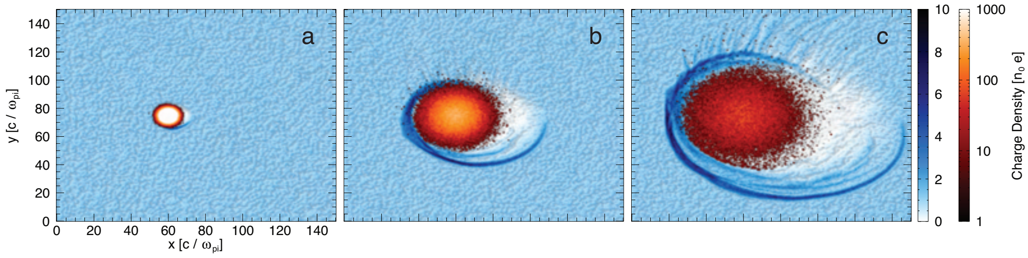


Figure 7: Charge density slice along the $xy$ plane at $z = 75$ at a) $t = 2.22$, b) $t = 11.08$, and c) $t = 19.94$. The solar wind charge density is represented in blue, and the Lithium plasma cloud charge density is represented in red.

$+y$ side of the expansion and the $-y$ side of the expansion, and shows that the maximum magnetic field intensity reached is over $1.4$, while the minimum magnetic field intensity is below $0.7$.

To understand the overall behavior of the system we analyze the evolution of both the electric field and the fluid velocity of the ions. From the inspection of the electric field in figure 3 and in figure 4, we see that outside of the cloud expansion zone the electric field vectors point in the $+y$ direction. This is in agreement with eq. 7, since the plasma is flowing in the $+x$ direction so that $-\vec{V_i} \times \vec{B}$ points in the $+y$ direction, and the magnetic field in this zone is uniform so that $\vec{J} = \vec{\nabla} \times \vec{B}$, in the second term of the equation, is mostly zero.

The electric field vectors in the plasma cloud dominated zone are curved in the counter-clockwise direction (figure 4), and the electric field intensity grows from the center of the cloud outwards. The explanation is related to the temperature-driven expansion of the plasma cloud. Figures 5 and 6 show an increase of the ion fluid velocity from the center of the cloud outwards, which is due to the fact that hotter ions diffuse outwards faster from their initial positions. Hence, the $-\vec{V_i} \times \vec{B}$ term once again explains both the counter-clockwise direction of the electric field and the electric field intensity growth outwards.

The spatial uniformity of the electric field, magnetic field, and plasma flow velocity and density, in the solar wind dominated zone, contrasts with the non-uniformity of the electric field in the plasma cloud expansion zone. In the later case, the spatial variation of the electric field yields a non-vanishing $\vec{\nabla} \times \vec{E}$ that drives the evolution of the magnetic field in time according to Faraday's law (eq. 12). The time evolution of the magnetic field results in the spatial non-uniformity of $\vec{B}$: the magnetic field enhancement in the $-x$ side and the magnetic field depletion on the $+x$ side. The $\vec{B}$ field non-uniformity in the cloud zone can then be interpreted as a current system, owing to $\vec{J} = \vec{\nabla} \times \vec{B}$, that acts as a diamagnetic current on the downstream side of the cloud.

The solar wind ions are affected by the electromagnetic structures formed by the cloud expansion, and the most visible effect is the asymmetry along the $y$ axis, which can be explained by the electric field configuration outside of the cloud zone and at the boundaries between the two zones. Looking at the electric field from figure 4, and at the charge density from figure 7, it can be seen that ions escape from the cloud mainly in the $+y$ side due to

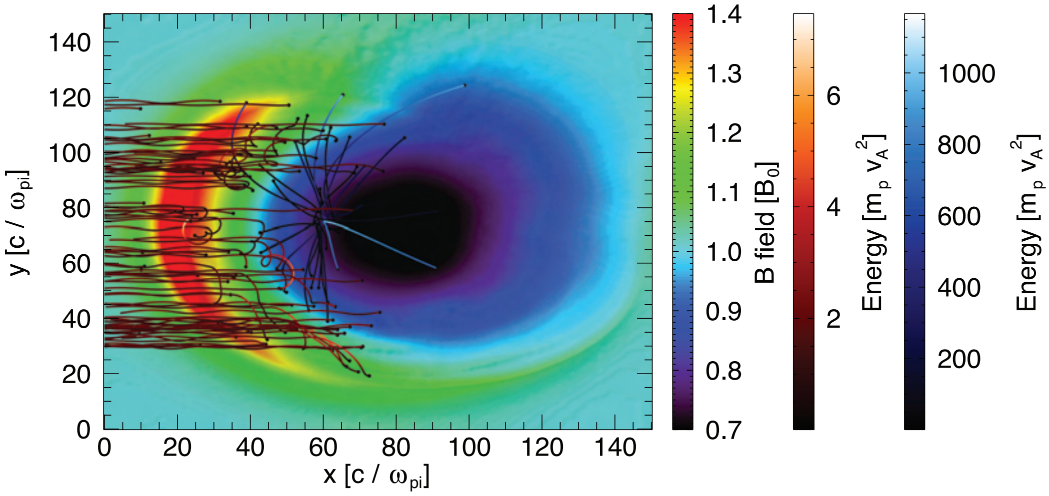


Figure 8: Slice along the $x\,y$ plane at $z = 75$ showing the magnetic field intensity, and a representative sample of particle tracks from the solar wind (red color table), and from the Lithium plasma cloud ions (blue color table). The line colors represent the energy of the particles.

the IMF-generated electric field that points in this direction. Also, the electric field points in opposite directions at the shock front boundary, leading to reconnection and turbulence.

Figure 7 also shows that the solar wind plasma is pushed out of the region where the Lithium plasma cloud dominates, forming a density bump that propagates outwards just in front of the plasma cloud expansion. This outer shock drives a smaller electric field present just outside the cloud boundary, seen in figure 4 to point in the $+x$ direction on the $-y$ side of the cloud. This electric field accelerates the solar wind ions present in this region, as can be observed in figure 6, while in the opposite side of the cloud it has a decelerating effect.

The trajectories of a sample of particles from the solar wind and from the Lithium cloud can be observed in figure 8. The $y$ axis asymmetry is patent once more in the solar wind particle trajectories that stream along the $-y$ side of the cloud, while particles impacting at higher $y$ are decelerated or back-scattered. The Lithium ions, on the other hand, escape the cloud in the $+y$ side, are picked up by the solar wind, and start to drift downstream.

These results demonstrate that the solar wind is effectively stopped from entering the Lithium dominated zone. This would not to be expected if we reasoned that a charged particle would be deflected only when its Larmor radius is small compared with the distance to the central object. In fact, in the unmagnetized scenario where the Larmor orbits are of the same order of magnitude of the central object (the cloud in this case, or the magnetic dipole field in the case described in the next section), this over-simplistic view must be abandoned. This aspect will be further explored in the next section, where we relate plasma flow deflection distances to the magnetic field intensity and plasma parameters such as the density and the plasma flow velocity.

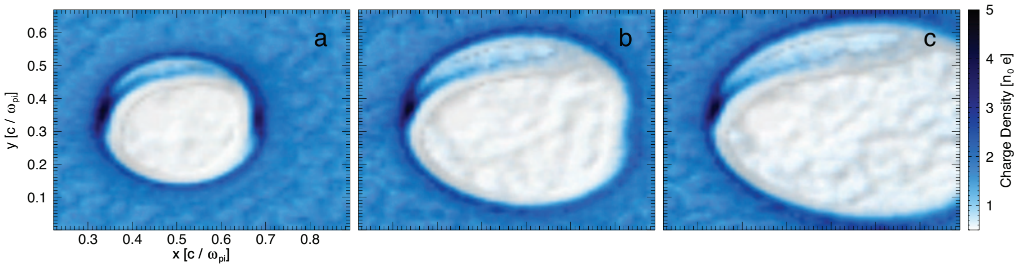


Figure 9: Density slice in the $x\,y$ plane at $z = 0.335$, in the middle of the simulation box, for times a) $t = 0.0952$, b) $t = 0.238$, and c) $t = 0.381$.

## 4 Mini-magnetosphere in the laboratory

Recent laboratory experiments were setup with the specific aim of studying particle deflection mechanisms, and studying the feasibility of protecting a spacecraft using a mini-magnetosphere [8]. In the final proposed configuration, the mini-magnetoshpere consists of a dipole magnetic field and a plasma source; the purpose of the plasma source is to expand the dipole magnetic field, which usually decays as $r^{-3}$, so that the decay is $r^{-\alpha}$ with $\alpha \sim 1$, thus increasing the efficiency of particle deflection [1].

In the current phase of the laboratory experiments, the dipole magnetic field is generated by a permanent magnet, and there is no plasma source inflating the magnetic field. A cylindrical magnet with radius $r_M = 13.5\,\mathrm{mm}$ is placed in a vacuum chamber, where it produces a magnetic field with a peak intensity of $B_{max} \approx 0.2\,\mathrm{T}$ at the edge of the magnet. A quasi-neutral proton/electron plasma beam with a number density of $n_b = 10^{12}\,\mathrm{cm}^{-3}$, a bulk velocity of $V_b = 400\,\mathrm{km\,s^{-1}}$, and a ion temperature of $T_b = 5\,\mathrm{eV}$, is then guided by an axial background magnetic field of intensity $B_b = 0.02\,\mathrm{T}$ towards the magnet.

For these reference parameters, the plasma flow has an acoustic Mach number of $M_{ac} = 12.91$, an Alfvènic Mach number of $M_a = 0.92$, and the Larmor radius of the ions is $r_{Lb} \sim 11.4\,\mathrm{mm}$, which corresponds to $r_{Lb}/r_M = 0.85$. The hybrid simulation method is then ideal for this configuration, since the ions are mostly unmagnetized in regions far from the magnet, and thus require a kinetic treatment.

Three sets of simulations were run in order to scan the dependency of the plasma stand-off distance, at the nose of the magnetopause in the beam propagation direction, with varying magnetic field intensity, with varying beam plasma density, and with varying plasma flow velocity. Simple MHD theory considers that the total pressure is conserved across the magnetopause, $\left[p + B^2/2\right] = 0$, where the first term is the plasma kinetic pressure and the second term is the magnetic pressure, and predicts that the distance from the magnetopause to the dipole origin is given by

$$r_{\mathrm{mp}} = \left(\frac{K\,B^2}{2\,n\,M\,V^2}\right)^{1/6} \tag{23}$$

where $B$ is the magnetic field intensity at the edge of the magnet, $n$ is the density, $M$ is the ion mass (protons), $V$ is the flow velocity of the plasma, and the parameter $K$ is a

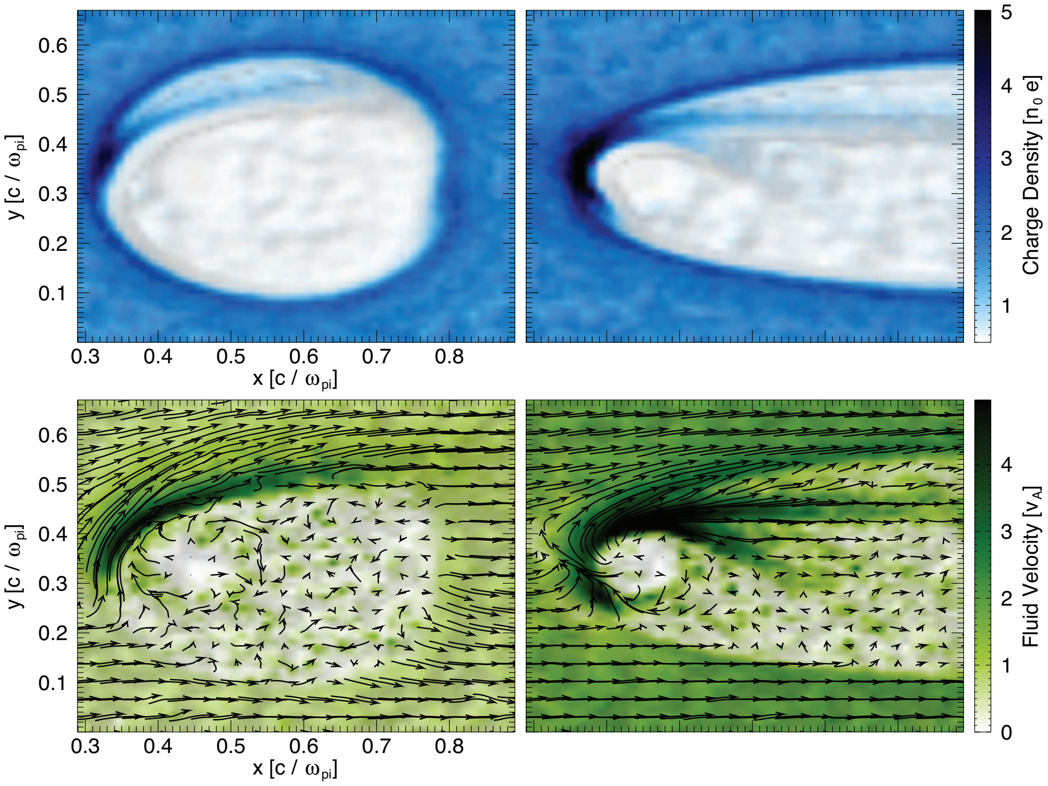


Figure 10: Density slice (top panel), and fluid velocity slice (bottom panel), in the $x\,y$ plane at $z = 0.355$, in the middle of the simulation box, for time $t = 0.2$. The left frames show the results for the reference simulation run, with $V_b = 0.92$, and the right frames show the results for a run with the same parameters but with $V_b = 2.84$.

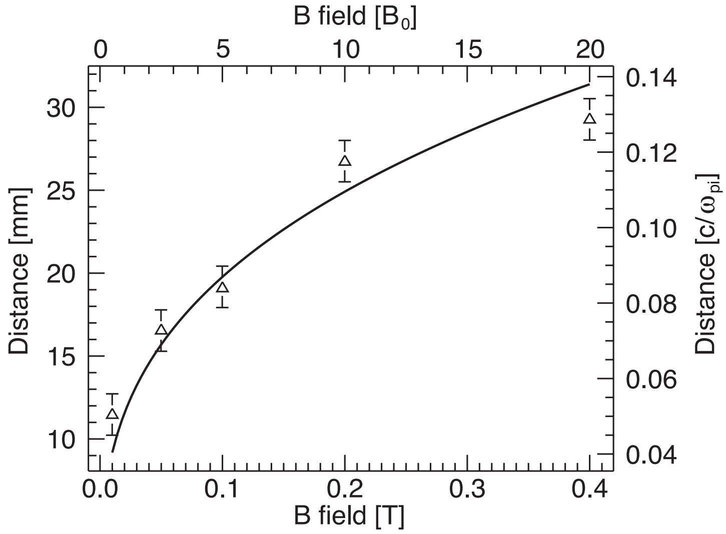


Figure 11: Distance of the mangetopause to the dipole origin, $r_{\mathrm{mp}}$, as a function of the magnetic field intensity at the edge of the permanent magnet. The solid line represents the theoretical prediction, eq. (23). The triangles represent the values measured in the simulations, with the error bars describing the resolution of the simulation.

free parameter of the theory accounting for the non-ideal specular reflection of the particles when hitting the magnetopause and deviations of the magnetic field intensity from its dipole field values [1, 29].

In our simulations the plasma flows along the background magnetic field in the $+x$ direction, and the magnetic dipole is centered in the middle of the simulation box, with the magnetic moment vector aligned along the $+z$ direction. The results presented are normalized to the simulation units, the density normalized to $n_0 = 10^{12}\,\mathrm{cm}^{-3}$, the spacial dimensions normalized to $c/\omega_{pi0} \approx 22.76\,\mathrm{cm}$, the time normalized to $\omega_{ci0}^{-1} \approx 0.52\,\mu\mathrm{s}$, the velocities normalized to $v_A \approx 436\,\mathrm{km\,s}^{-1}$, the magnetic field normalized to $B_0 = 0.02\,\mathrm{T}$, and the electric field normalized to $B_0\,v_A \approx 8732\,\mathrm{V\,m}^{-1}$. The box size is $0.89\,\mathrm{c}/\omega_{\mathrm{pi0}} \approx 20.35\,\mathrm{cm} \approx 17.83\,\mathrm{r_{Lb}}$ in the $x$ direction, $0.67\,\mathrm{c}/\omega_{\mathrm{pi0}} \approx 15.26\,\mathrm{cm} \approx 13.37\,\mathrm{r_{Lb}}$ in the $y$ and $z$ directions, and $80 \times 60 \times 60$ grid cells are used, yielding a cell size of $\Delta \approx 0.011\,\mathrm{c}/\omega_{\mathrm{pi0}} \approx 2.5\,\mathrm{mm} \approx 0.22\,\mathrm{r_{Lb}}$. The time step is $\Delta t \approx 9.52 \times 10^{-7}\,\omega_{\mathrm{ci0}}^{-1} \approx 0.5\,\mathrm{ps} \approx 1.52 \times 10^{-7}\,\mathrm{T_{Lb}}$, and the simulation is run up to $400\,\mathrm{k}$ time steps, which results in a total simulation time $T \approx 0.38\,\omega_{\mathrm{ci0}}^{-1} \approx 0.2\,\mu\mathrm{s} \approx 0.06\,\mathrm{T_{Lb}}$. We use 27 particles per cell to model the beam.

The reference simulation for our parameter scans is the run reproducing the laboratory parameters. We can see in figure 9 a cut of the density evolution of the plasma beam for this run. At early times, the magnetic dipole field acts as a magnetic piston, and the plasma is expelled from the most intense magnetic field region near the dipole origin. Here, the dipole magnetic field plays the role of the Lithium cloud in the previous section, while the plasma beam plays the role of the solar wind. At some point during the early stages of the simulation, the beam kinetic pressure equalizes the outward magnetic pressure, and the

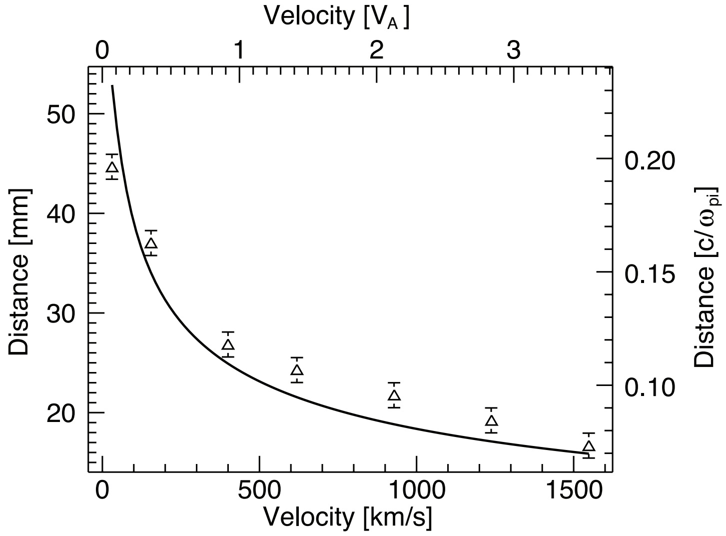


Figure 12: Dependence of the distance of the magnetopause to the dipole origin, $r_{\rm mp}$, on the density of the plasma flow, for the baseline simulation parameters. The solid line represents the theoretical prediction, eq. (23). The triangles denote the simulation results, with the error bars describing the resolution of the simulation.

magnetopause is formed according to eq. 23. A direct measurement of $r_{\rm mp}$ in the laboratory yielded $r_{\rm mp} = 28.5\,\mathrm{mm}$, and the same measurement in the reference simulation yields $r_{\rm mp} = 26.7\,\mathrm{mm} \pm 2.5\,\mathrm{mm}$, showing a good agreement between the two. The uncertainty in the simulation measurement is due to the simulation grid cell size.

Figure 10 shows a comparison between the reference run, and a run with the same parameters but $V_b = 2.84$, highlighting the bow shock shape and the fluid velocity vectors. The width of the bow shock is narrowed in the transverse direction, in the second run, comparing to the reference run, but the qualitative behavior of the two scenarios is very similar. In particular, there is a particle flow, present in both cases, that penetrates to some degree the bow shock boundary and that enables some particles to enter the density-depleted zone. Looking at the velocity vectors in the central region also indicates that this low density plasma is turbulent, and the observation of the same behavior in both cases indicates that the phenomenon represents a characteristic feature of the problem and not a numerical artifact due to the specific plasma parameters used. A similar effect is observed in the laboratory experiment [1], where particles penetrate the bow shock through a magnetic cusp; however, as a definite physical explanation for the phenomena is lacking, it is not trivial to infer a relation between the two observations.

In the first simulation scenario, we have scanned the magnetic field intensity, with the magnetic field on the edge of the magnet varying from $0.01\,\mathrm{T}$ to $0.4\,\mathrm{T}$, while keeping the reference run plasma parameters fixed. In figure 11, $r_{\rm mp}$ measured in the simulation is compared with the theoretical prediction from eq. 23. The qualitative behavior is obtained, but some quantitative discrepancies are visible, with better agreement being obtained for

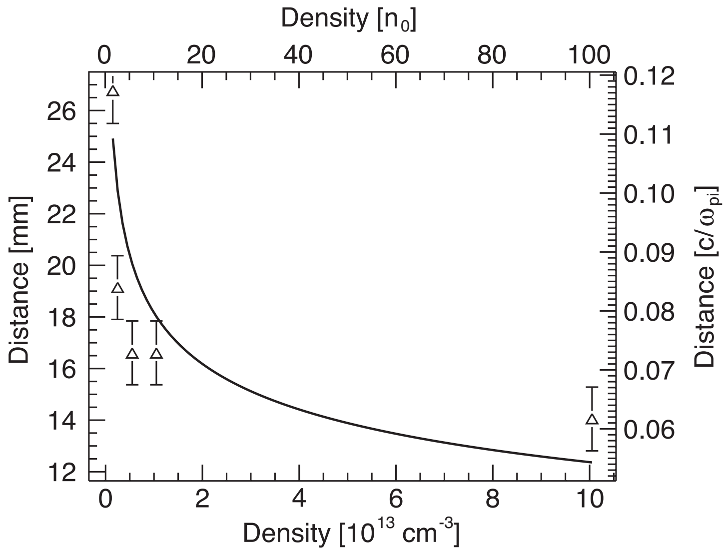


Figure 13: Distance of the magnetopause to the dipole origin, $r_{\mathrm{mp}}$, as a function of the plasma flow velocity, for the baseline simulation parameters. The solid line represents the theoretical prediction, eq. (23). The triangles denote the simulation results, with the error bars describing the resolution of the simulation.

lower magnetic pressures.

Scanning the distance $r_{\mathrm{mp}}$ as a function of the plasma density, figure 12, the qualitative behavior is recovered, with a slight deviation from the theoretical model, as in the previous scenario. For the plasma densities scanned, the $\beta$'s range from $0.005$ to $0.5$. The scaling $r_{\mathrm{mp}} \propto n^{-1/6}$, from eq. 23, indicates that $r_{\mathrm{mp}}$ depends weakly on the density, while it is strongly affected by variations of the magnetic field, $r_{\mathrm{mp}} \propto B^{1/3}$, and by variations of velocity, $r_{\mathrm{mp}} \propto v^{-1/3}$, which means that more significant changes of $r_{\mathrm{mp}}$ are observed in these cases for our parameter scan, and for our numerical parameters.

Finally, in the third scenario, the velocity of the solar wind was varied from $30.97\,\mathrm{km/s}$ up to $1548\,\mathrm{km/s}$, corresponding to acoustic Mach numbers from $M_{ac} = 1$ to $M_{ac} = 50$ and Alfvènic Mach numbers from $M_a = 0.07$ to $M_a = 3.5$. The results, depicted in figure 13, follow the same behavior as in the previous scenarios, with a small deviation from the theoretical values for most of the measured points. For all the simulation scenarios the value for $K$, in eq. 23, was $K = 6.09 \times 10^{-12}\,\mathrm{m}^6$ adjusted from the data.

The discrepancies between measured simulation values and the theoretical values of eq. 23 are associated with the simplifying assumptions of the theoretical model. In particular, in the derivation of eq. 23, the thermal pressure is neglected, and the Rankine-Hugoniot shock jump conditions are implicitly used [29]. Neglecting the thermal pressure causes deviations for low values of the velocity $V$ observed in figure 13, and the use of the Rankine-Hugoniot jump conditions implies considering a simple one fluid magnetohydrodynamics model, which has limited applicability in this problem, as finite Larmor radius effects are not negligible.

## 5 Discussion and conclusions

We analyze two different plasma interaction scenarios, relevant for ongoing research on spacecraft protection against energetic charged particles. Unlike the case of the solar wind interaction with a planetary magnetosphere, such as the Earth magnetosphere where $r_{Lsw}/r_{\oplus} \sim 0.01$ ($r_{\oplus} \equiv$ radius of the earth), the Larmor radius of the solar wind ions and the Larmor radius of the beam protons are of the same order of magnitude of the system sizes. While in the Earth/solar wind case MHD simulations can model most phenomena of interest on a global scale, the same does not hold true for these smaller systems [30].

The numerical modeling of the AMPTE release experiments, as analyzed in section 3, shows that a thermally expanding plasma cloud is capable of effectively deflecting the solar wind. The expansion of the cloud against the incoming solar wind compresses and enhances the magnetic field at the shock interface, while the magnetic field downstream is depleted and a diamagnetic cavity is formed. The solar wind particles are deflected mostly sideways, in the $-y$ direction, and some of these particles are accelerated up to twice their initial bulk velocity, due to the electric field generated by the radially propagating plasma cloud.

In the laboratory scenario, the dipole magnetic field acts as a magnetic piston to create a plasma depleted cavity, as in the cloud expansion case. In this case the differences between the experimental setup and typical space plasma parameters should be considered. The two main differences reside in the number density of the solar wind, typically $\approx 5\, cm^{-3}$ at 1 AU, and in the typical value for the IMF which is $\approx 10\,\mathrm{nT}$ at 1 AU, representing much lower values than the ones used in the laboratory. These differences result in a plasma $\beta \sim 0.4$, and a typical acoustic Mach number of $M_{ac} \sim 7.3$, and an Alfvènic Mach number $M_a \sim 4.6$, that should be compared with values of $\beta \sim 0.005$, $M_{ac} \sim 12.9$, and $M_a \sim 0.9$, respectively, for the laboratory case. Assuming that the magnetic field intensities of a system on-board of a spacecraft can be of the order of magnitude of the ones tested in the laboratory, the system should stop the incoming solar wind at longer $r_{\mathrm{mp}}$, according to eq. (23), by a factor of $(n/n_{sw})^{1/6} \sim 76$ resulting in a standoff distance of a few meters.

In order to push the concept of the mini-magnetosphere further, the injection of plasma in the region of the dipole field to expand the magnetic field has to be considered. This plasma injection can result in a change of the decay law from $r^{-3}$ to $r^{-\alpha}$, with $\alpha \sim 1$, as outlined before. An estimate of operating parameters for this configuration is calculated based on the requirement of deflecting $1\,\mathrm{MeV}$ protons and considering a magnetic field intensity decay of $r^{-1}$. For efficient reflection, we require the Larmor radius to be a fraction, $f \sim 20\%$, of the distance of the proton to the spacecraft, yielding a magnetic field intensity of $0.72\,\mathrm{T}$ generated by a current loop with $r = 1\,\mathrm{m}$, corresponding to a magnetic moment $M \sim 7.2 \times 10^6\,\mathrm{A\,m}^2$.

The above estimates provide only a crude approximation; our results indicate that the requirements for the magnetic field intensity can be relaxed in the self-consistent configuration. As observed in both simulation scenarios, even when $r_{Lsw}$ and $r_{Lb}$ are comparable, respectively, to the radius of the cloud and to $r_{\mathrm{mp}}$, the incoming plasma is efficiently deflected.

Future work on the subject will focus on the behavior of a mini-magnetosphere in a space plasma environment, accounting for the much lower density of the solar wind. The injection of plasma and the expansion of the dipolar magnetic in the presence of the solar wind flow will also be tested. The deflection of energetic particles by these systems will be considered, resorting to test particles and following particle trajectories in time, thus providing information that will allow for a detailed assessment of the role of mini-magnetospheres in the space environment.

## 6 Acknowledgments

This work was supported by Fundação para a Ciência e a Tecnologia (FCT/Portugal) under grant SFRH/BD/17750/2004. The simulations presented in this paper were produced using the IST Cluster (IST/Portugal).

## References

[1] L. Gargaté, R. Bingham, R. A. Fonseca, R. Bamford, A. Thornton, K. Gibson, J. Bradford, L. O. Silva, Plasma Phys. Control. Fusion 50, 074017, 2008

[2] R. M.Winglee, J. Slough, T. Ziemba, A. Goodson, J. Geophys. Res., 105(A9), 21067, 2000

[3] J. T. Mendonça, A. L. Brinca, R. Fonseca, J. Loureiro. L. O. Silva, I. Vieira, J. of Plasma Phys. 71, 4, 495, 2005

[4] J. Loureiro, J. T. Mendonça, A. L. Brinca, R. Fonseca, L. O. Silva, I. Vieira, J. of Atmosph. and Solar-Terrestrial Phys. 67, 14, 1315, 2005

[5] T. Ziemba, R. Winglee, P. Euripides, J. Slough, $43^{rd}$ APS DPP meeting, KP1.061, 2001

[6] R. M. Winglee, T. Ziemba, P. Euripides, J. Slough, AIP Conference Proceedings, 608, 433, 2002

[7] I. Funaki, H. Kojima, H. Yamakawa, Y. Nakayama, Y. Shimizu, Astrophysics and Space Science, 307, 1-3, 63, 2007

[8] R. Bamford, K. J. Gibson, A. T. Thornton, J. Bradford, R. Bingham, L. Gargaté, L. O. Silva, R. A. Fonseca, M. Hapgood, C. Norberg, T. Todd, R. Stamper, $35^{th}$ EPS Conference Proceedings, Plasma Phys. Control Fusion, in press

[9] D. Winske, N. Omidi, Phys. of Plasmas 12, 072514, 2005

[10] H. Tang, J. Yao, H. Wang, Y. Liu, Phys. of Plasmas 14, 053502, 2007

[11] F. Kazeminezhad, Hybrid Modeling of Plasmas and Applications to Fusion and Space Physics, UCLA PhD thesis, 1989

[12] A. Valenzuela, G. Haerendel, H. Foeppl, F. Melzner, H. Neuss, Nature, 320, 700, 1986

[13] G. Haerendel, G. Paschmann, W. Baumjohann, C. W. Calrson, Nature, 320, 720, 1986

[14] S. C. Chapman, S. J. Schwartz, J. Geophys. Res. 92(A10), 11059, 1987

[15] J. B. Harold, A. B. Hassam, Geophys. Res. Letters 18 (2), 135, 1991

[16] P. A. Delamere, D. W. Swift, H. C. Stenbaek-Nielsen, Geophys. Res. Letters 26 (18), 2837, 1999

[17] P. A. Bernhardt, R. A. Roussel-Dupre, M. B. Pongratz, G. Haerendel, A. Valenzuela, D. A. Gurnett and R. R. Anderson, J. Geophys. Res. 92(A6), 5777, 1987

[18] A. B. Hassam and J. D. Huba, Geophys. Res. Letters 14, 60, 1987

[19] R. Bingham, V. D. Shapiro, V. N. Tsytovich, U. de Angelis, M. Gilman and V. I. Shevchenko,Phys. Fluids B 3, 1728, 1991

[20] J. M. Dawson, Rev. Mod. Phys. 55, 403, 1983

[21] C. K. Birdsall, A. B. Langdon, Plasma Physics Via Computer Simulation, Institute of Physics Publishing, Bristol and Philadelphia, 1998

[22] L. Gargaté, R. Bingham, R. A. Fonseca, L. O. Silva, Comp. Phys. Commun., 176, 419, 2007

[23] R. A. Fonseca, L. O. Silva, F. S. Tsung, V. K. Decyk, W. Lu, C. Ren, W. B. Mori, S. deng, S. Lee, T. katsouleas, J. C. Adam, Lecture Notes on Computer Science 2331, 342, Springer-Verlag, Heidelberg, 2002

[24] A. S. Lipatov, The Hybrid Multiscale Simulation Technology, Springer, 2002

[25] V. K. Decyk, S. R. Karmesin, A. de Boer, P. C. Liewer, Comp. in Phys., 10 (3), 1996

[26] K. S. Yee, IEEE Trans. Ant. Prop. 14 (3), 302, 1966

[27] J. P. Boris, Proc. Fourth Conf. Num. Sim. Plasmas, Naval Res. Lab, 3-67, 1970

[28] M. Snir, S. Otto, S. Huss-Lederman, D. Walker, J. Dongarra, MPI - The Complete Reference, MIT press, 1999

[29] W. Baumjohann, R. A. Treumann, Basic Space Plasma Physics, Imperial College Press, 2004

[30] F. Kazeminezhad, J. M. Dawson, R. Bingham, J. Geophys. Res. 98 (A6), 9493, 1993